Advanced Materials

ADVANCED MATERIALS
www.advmat.de

RESEARCH ARTICLE

A Bifunctional Colloidal Quantum Dot Diode for Nanosecond Short-Wave Infrared Detection and Emission

Yu-Hao Deng[1,2] | Dobromił Respekta[1,2] | Jing Bai[1,2] | Korneel Molkens[1,2,3,4] | Ezat Kheradmand[1,2] | Chao Pang[2,3] | Robin R. Petit[5] | Pepijn Verscheure[1,2] | Philippe B. Green[1,2] | Elaheh Teymouri[1,2] | Christophe Detavernier[5] | Dries Van Thourhout[2,3] | Pieter Geiregat[1,2,4] | Zeger Hens[1,2,4]

[1]Physics and Chemistry of Nanostructures Group, Ghent University, Gent, Belgium | [2]Center For Nano and Biophotonics, Ghent University, Gent, Belgium | [3]Photonics Research Group, Ghent University - IMEC, Gent, Belgium | [4]Core Facility for Non-linear Microscopy and Spectroscopy, Gent, Belgium | [5]Department of Solid State Sciences, CoCooN, Ghent University, Gent, Belgium

Correspondence: Yu-Hao Deng (yuhao.deng@ugent.be) | Zeger Hens (zeger.hens@ugent.be)

Received: 9 December 2025 | **Revised:** 4 June 2026 | **Accepted:** 29 June 2026

Keywords: colloidal quantum dots | light-emitting diode | photodetector | short-wavelength infrared | ultrafast

ABSTRACT

Short-wave infrared (SWIR) technologies are vital for optical communication, all-weather imaging, and advanced spectroscopy. Using a single diode for light detection and emission can reduce device footprints, lower cost and enable fast, bidirectional communication. However, dual detection/emission operation often involves incompatible choices of material and stack design, which result in devices with inferior performance. Here, we introduce a bifunctional PbS QD diode stack that achieves, for the first time, nanosecond-fast photodetection and emission in a single SWIR device. Using thin active layers with high charge-carrier mobility and compact geometries, we demonstrate a record 2 ns response in photodiode (QDPD) mode and 11.7 ns rise time/6.5 ns fall time in light-emitting diode (QDLED) mode. This high-speed operation is combined with a 49% external quantum efficiency (EQE) and 2.6×10^{12} cm·Hz$^{0.5}$·W^{-1} detectivity for QDPD operation, while the QDLED reaches 8.1% EQE. These high-speed, compact devices unify imaging and detection with a single, CMOS-compatible platform, and set the stage for integrated SWIR photonics and bidirectional optical interconnects. This work demonstrates the potential of QDs to unify imaging, detection, and communication in a single materials platform.

1 | Introduction

Short-wave infrared light (SWIR, 1000–3000 nm) is safe for the human eye, provides chemical information about objects, and is far less affected by scattering than visible light [1–4]. By enabling enhanced imaging, SWIR technology has moved beyond long-distance data communication to new applications, such as light detection and ranging (LiDAR), augmented reality (AR), biomedical imaging and environmental monitoring [5–9]. The growing demand of such applications for low-cost, small-footprint optoelectronics with high-frequency operation and low power consumption can be met by single, bifunctional devices capable of both detecting and emitting SWIR light. Furthermore, bifunctional detection/emission modules can strongly reduce interconnect latency and power consumption in photonic chips, and would represent a key step toward truly monolithic on-chip optoelectronic integration, resolving a persistent bottleneck in current platforms [10, 11].

Conventional SWIR technology makes use of epitaxially grown compound semiconductors, like (In, Ga) As, for detecting or emitting SWIR light. Broadband SWIR detection is possible using a single ternary composition—$In_{0.53}Ga_{0.47}As$—that is lattice-matched to InP substrates, and external quantum efficiencies

(EQE) close to 100% have been reported [12]. Emission, on the other hand, is narrowband, and lattice-matched quaternary (In, Ga) (As, P) with variable composition is needed to tune the central wavelengths, where EQEs are typically around 1%–5% [13, 14]. Considering bifunctional devices, such variations in material composition come on top of different device designs, either aimed at maximizing light absorption and charge carrier extraction in photodiodes, or radiative recombination and light outcoupling in emitters. As a result, SWIR emitters and detectors are typically separate components that are combined with silicon photonic chips, readout or driver circuits by heterogeneous integration, like flip-chip bonding, which raises device complexity and production cost.

Colloidal quantum dots (QDs) offer a promising alternative to conventional SWIR semiconductors [4, 15–18]. The quantum confinement effect in QDs enables precise control over the emission wavelength and the absorption onset across a wide spectral range [18–21]. Moreover, QD dispersions are solution processable, which allows the formation of QD films on a variety of substrates without lattice-matching requirements by means of CMOS-compatible fabrication techniques, like spin coating or inkjet printing [22]. These advantages make QDs an ideal platform for scalable and multifunctional SWIR optoelectronic devices, as demonstrated, for example, by the development of SWIR imagers, LEDs and lasers based on PbS QDs [23–25], and the recent effort to extend such results to Pb-free QDs, such as InAs and InSb [18, 26–28]. By now, QD photodiodes (QDPDs) can reach ns response times [4], and SWIR imagers meet industry standards [29]. Furthermore, building on progress in QDPD efficiency, the external quantum efficiency (EQE) of electroluminescent QDLEDs has gradually increased to 11.8% [24, 30, 31]. On the other hand, these QDLEDs only reach bandwidths of ∼1 MHz, and bifunctional stacks operating as QDPD and QDLED are considered less feasible as both devices require different QD layer thickness for optimal operation [10, 11].

Here, we demonstrate a bifunctional SWIR diode—integrated within a single ultrathin PbS QD stack through one unified process flow—that delivers nanosecond-fast and highly efficient performance as both a QDPD and a QDLED, depending on the applied bias. We first outline that stack innovations leading to fast and efficient photodetection—ultrathin QD films with high charge carrier mobility, absorption enhancement through a dielectric cavity—align with the design principles for a fast and efficient QDLED. Next, we introduce a film fabrication method that reduces residual organic contamination and increases charge carrier mobility. By this method, we form a *p*–*n* junction in the PbS QD film with a 50 nm thick active layer, and demonstrate that this stack operates as a QDPD with a 2 ns response time and a QDLED with nanosecond rise and fall times. Importantly, the stack combines this fast response with state-of-the-art efficiency in both operation modes, realizing a QDPD and a QDLED with 49% and 8.1% EQE, respectively. This result shows that QD technology can realize bifunctional operation, in contrast to III-V technology, and sets new performance benchmarks for SWIR QDPDs, QDLEDs and bifunctional QD devices. In particular, the realization of high-speed photodetection and light emission in a single, solution-processed chip opens new avenues for compact, low-cost imaging, sensing, emission and communication applications in next-generation integrated SWIR systems.

1.1 | Design Rules for High-Speed Dual QD Photodetector and LED

QDPDs and QDLEDs are formed using similar stacks, in which charge transport layers contact both sides of a QD film that is used as light absorber or emitter, see Figure 1a. Even so, to enhance the EQE, QDPDs typically use QD films that are several hundreds of nm thick, while QDLEDs stacks involve layers only a few QDs thick [24]. Hence, while the idea of bifunctional QDPD/QDLED operation has been demonstrated using CdSe-based nanorods for absorbing and emitting visible light, the photodetector responsivity of bifunctional QD stacks is modest [10].

Recently, design principles were outlined and implemented for high-speed and efficient SWIR photodetection. Building on established methods to form an internal *p*–*n* junction within a PbS QD film, key aspects were (1) using ultrathin (50 nm) *n*-PbS QD films with high electron mobility to promote rapid drift of charge carriers, (2) reducing the contact pad area to minimize capacitive delays, and (3) enhancing light absorption by turning the QDPD stack into a dielectric cavity that maximize the electric field in the QD film. Points (1) and (2) follow from the expression of the response time τ_{res} of such a thin stack as the combination of the drift time (τ_{drift}) and the *RC* time constant (τ_{RC}):

$$\tau_{\mathrm{res}} = \sqrt{\tau_{\mathrm{drift}}^2 + 2.2\tau_{\mathrm{RC}}^2} \tag{1}$$

In this expression, the carrier lifetime is neglected under the assumption that the photogenerated carriers in a fully depleted, high-field geometry are swept out before significant recombination occurs, while a factor 2.2 is added since the response time involves the variation of the photocurrent between 10% and 90% of the maximal value [19]. As outlined in Section S1, and shown in Figure 1b, τ_{res} can reach a ns regime for 50 nm thick films with a charge carrier mobility of 0.1 $\mathrm{cm}^2/(\mathrm{V}\cdot\mathrm{s})$ and a circular contact pad with a 50 μm diameter.

For a QDLED, the response time will similarly depend on the *RC* time of the entire stack, and the internal time constants related to the drift (τ_{drift}) and luminescent recombination (τ_{PL}) of charge carriers within the active layer. As outlined in Section S2, the internal time constants combine to a single electroluminescent time constant τ_{EL}: [32]

$$\tau_{\mathrm{EL}} = \frac{\tau_{\mathrm{drift}}\tau_{\mathrm{PL}}}{\tau_{\mathrm{drift}} + \tau_{\mathrm{PL}}} \tag{2}$$

This electroluminescent lifetime will dominate the QDLED response time under conditions where the *RC* time of the entire stack is sufficiently short. As can be seen from Equation (2)and Figure 1c, τ_{EL} will always be shorter than either τ_{drift} and τ_{PL}, and minimizing both time constants will yield a QDLED with the fastest possible response.

The drift time can be expressed in terms of the charge carrier mobility, the layer thickness, and the voltage drop across the QD film:

$$\tau_{\mathrm{drift}} = \frac{d^2}{\mu V} \tag{3}$$

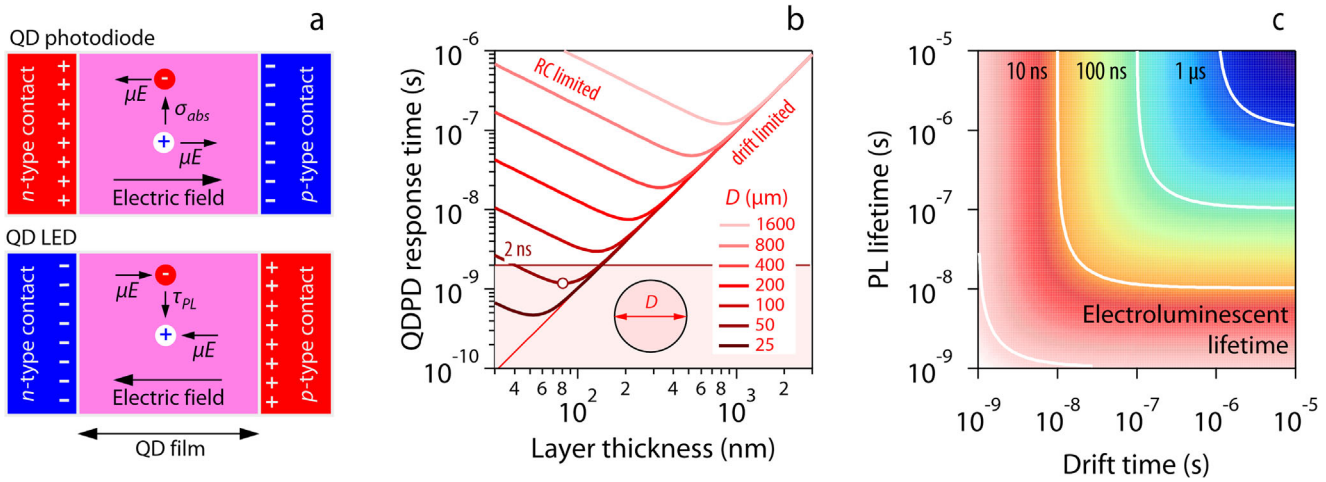

FIGURE 1 | Response time estimation. (a) Scheme of (top) a QDPD stack consisting of a fully depleted photo-active layer for which the mobility μ and the electric field $E = V/d$ determine the drift time and (bottom) a QLED stack for which the drift time and the photoluminescent lifetime determine the electroluminescent time constant. (b) QDPD response time determined from the combination of the RC time and the drift time as a function of the thickness of the QD film. Different device areas are considered, as indicated. Charge carrier mobility is taken as 0.1 $cm^2/(V \cdot s)$ and the potential drop across the QD film as 1 V. The shaded area highlights response times shorter than 2 ns. (c) Color map of the electroluminescence lifetime as a function of the drift time and the photoluminescence lifetime. White lines represent contours as indicated.

Hence, minimizing τ_{EL} through τ_{drift} is possible by reducing the QD film thickness and increasing carrier mobility. Similarly, τ_{PL} can be written in terms of an intrinsic lifetime $\tau_{PL,0}$ and the local field factor f_{LF}, which expresses the ratio between the electric field within and outside a QD [33]:

$$\tau_{PL} = \frac{\tau_{PL,0}}{|f_{LF}|^2} \tag{4}$$

For PbS QDs in apolar solvents, $|f_{LF}|^2$ can be as small as 0.07 [34], due to the large contrast between the dielectric constant of PbS and the surroundings. As a result, dispersed PbS QDs have a long PL lifetime of ≈1 μs [35]. However, $|f_{LF}|^2$ can be enhanced by increasing the dielectric constant of the surroundings—as is the case in a densely-packed QD film—and by placing QDs in the high-field region of a (dielectric) cavity. We thus conclude that stack modifications meant to achieve short response times in a QDPD structure—densely packed QD films, dielectric cavity enhancement—are fully aligned with the requirements to minimize τ_{EL} in a QDLED; a most promising outlook for bifunctional devices.

1.2 | Formation of QD Films With Internal *p–n* Junction

Following the design rules, thin QD films with high charge carrier mobility are needed for realizing efficient, high-speed bifunctional devices. A well-established procedure to obtain high carrier mobility in PbS QD films is replacing the long organic ligands that passivate as-synthesized QDs by short moieties through ligand exchange [22]. As depicted in Figure 2a, solid-state ligand exchange involves the post-deposition extraction of the organic ligands from a QD film through exposure to a ligand-exchange solution. The approach enables formation of heterojunctions with precise thickness control [36], where tetrabutylammonium iodide (TBAI) and ethanedithiol (EDT) are ligands known to form *n*-type and *p*-type QD films, respectively [37]. However, incomplete ligand replacement can limit charge-carrier mobilities, while switching from TBAI to EDT exposure can undo to *n*-type character of the initially deposited film, an effect that hampers the formation of ultrathin *p-n* junctions in PbS QD films [38].

The alternative is the formation of films from QD inks stabilized by the intended ligand, see Figure 2a. We followed this solution-exchange approach to fabricate *n*-PbS QD films as part of a bifunctional device stack [39]. This film was formed on top of an *n*-type ZnO electron transport layer using PbS QDs with a bandgap absorption at 1330 nm, see Section S3 for QD characteristics. On top of this film, a layer of *p*-PbS QDs with a bandgap absorption at 950 nm was deposited using solid-state exchange with EDT, which was terminated by a gold contact evaporated through a shadow mask. The PbS QDs were synthesized by reacting lead oleate with a substituted thiourea, following a previously reported procedure [40], and purified sufficiently using four precipitation/resuspension cycles to remove residual ligands as detailed in Section S3. As outlined in the **Methods** section, the *n*-PbS QD inks were prepared in dimethylformamide using a mixture of metal halides and acetate salts as the stabilizing moieties.

To assess the quality of QD films made through solution ligand exchange, we compared *n*-PbS QD films formed by solution exchange with films subjected to a similar ligand exchange through a solid-state method [4]. Figure 2b displays the Fourier-transform infrared spectrum of equally thick PbS QD films made of as-synthesized QDs, and through solid-state and solution exchange. Using the intensity of the C–H vibration as a measure for the amount of oleate ligands in the film, one sees that films made through solid-state ligand exchange still contain measurable amounts of this initial ligand, while films from pre-exchanged QD inks are in essence free of residual oleate. Furthermore, by preventing the volume shrinkage related

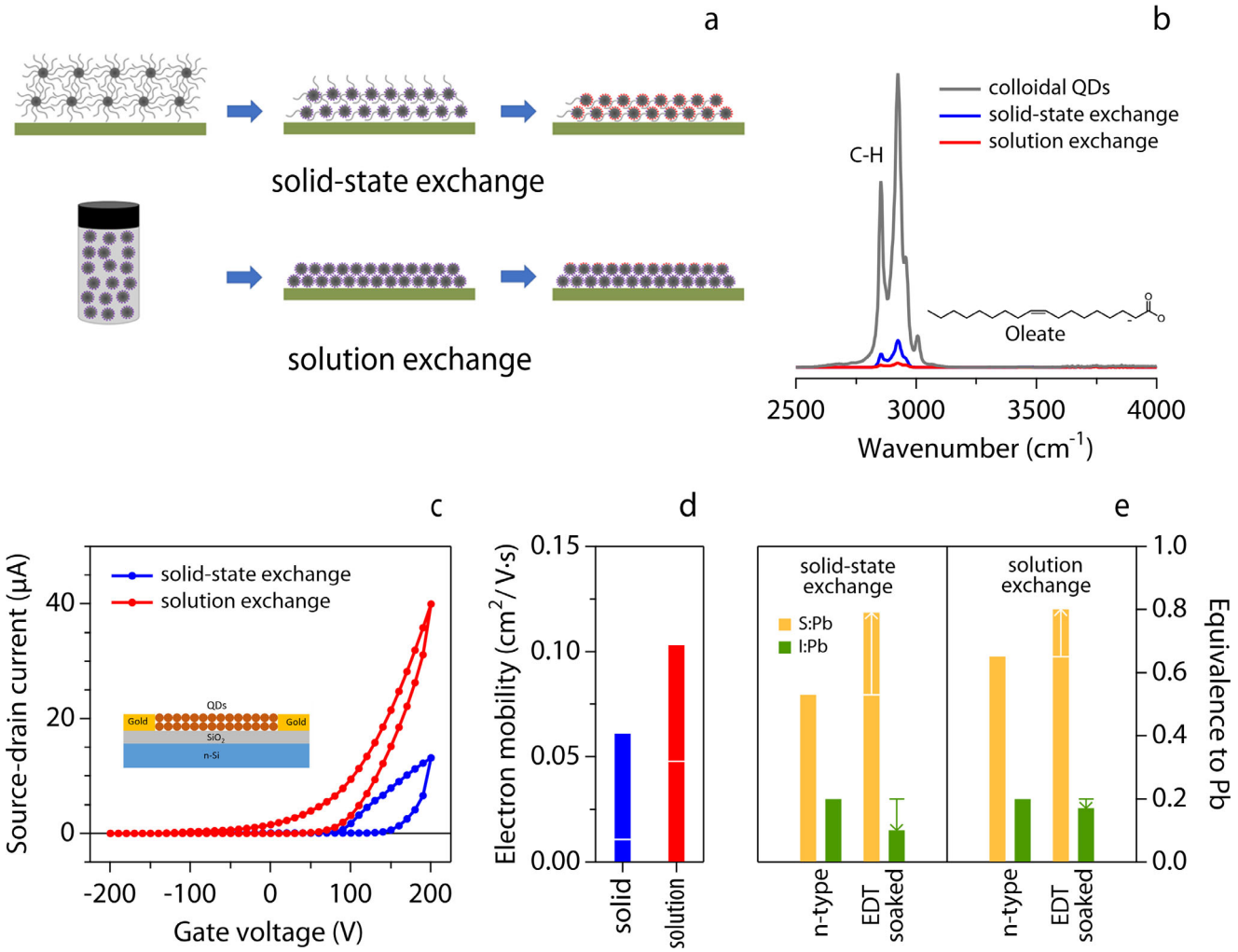

FIGURE 2 | **Formation of QD films**. (a) Depiction of the different methods used to fabricate a stack of ultrathin *n*-PbS QD films, indicating that solution exchange removes oleic acid ligands more efficiently and results in more compact film than solid-state exchange. (b) Infrared spectrum films of (grey) as-synthesized colloidal PbS QDs, and films formed through (blue) solid exchange and (red) solution exchange films. All films were formed using similar spin-coating conditions. (c) Transfer curves for *n*-type PbS QD films formed through (blue) solid and (red) solution exchange. (d) Electron mobility for both types of films derived from (white strip) forward and (full bar) backward scan. (e) (Orange) S:Pb and (green) I:Pb ratio in (*n*-type) an initially formed *n*-type PbS QD films and (EDT soaked) after soaking in an EDT solution.

to the extraction of oleic acid, solution exchange results in more uniform films with no visible cracks and sub-nanometer surface roughness, see Section S4. Furthermore, we evaluated the electron mobility in the *n*-PbS films using field-effect transistor measurements. As shown in Figure 2c,d and Section S5, both films show clear evidence of electron conductivity, while solution-exchanged films show less hysteresis and a higher mobility in the forward and backward scan—up to 1.03×10^{-1} cm^2/ (V · s)—than films made through solid-state exchange (Table S2). Note that these figures should be considered as lower limits, as any imperfections in the film will reduce the source-drain current, and the analysis assumes that variations in the gate voltage add or remove only mobile charge carriers within the QD film. This result may indicate that the solution-phase protocol better passivates deep-level traps and minimizes parasitic charge accumulation. Finally, we analyzed the change in film composition following the exposure of an initially formed *n*-type QD film to EDT. As can be seen in Figure 2e, this treatment leads to a considerable reduction of the iodine content and a pronounced increase of the sulfur content of the film in the case of solid-state ligand exchange. These changes have been attributed to iodide leaching from the underlying *n*-PbS film [41], and can disrupt the *p*-*n* junction [4, 42] However, when the *n*-type film is formed using a pre-exchanged ink, the changes in composition are minor. This difference probably reflects the formation of a denser film, and allows the direct formation of a *p*-type PbS film without risk of disrupting the underlying layer.

1.3 | Nanosecond-Response Photodiode Under Detection Mode

As Figure 3a illustrates, we formed QDPD stacks through the sequential deposition of a 50 nm *n*-type PbS and a 50 nm *p*-type PbS QD films as the active layer, that was sandwiched between a Glass/ITO/ZnO substrate contacting the *n*-type part, and a gold electrode contacting the *p*-type part. In such a stack, the EDT-treated p-PbS QD film acts as an additional electron

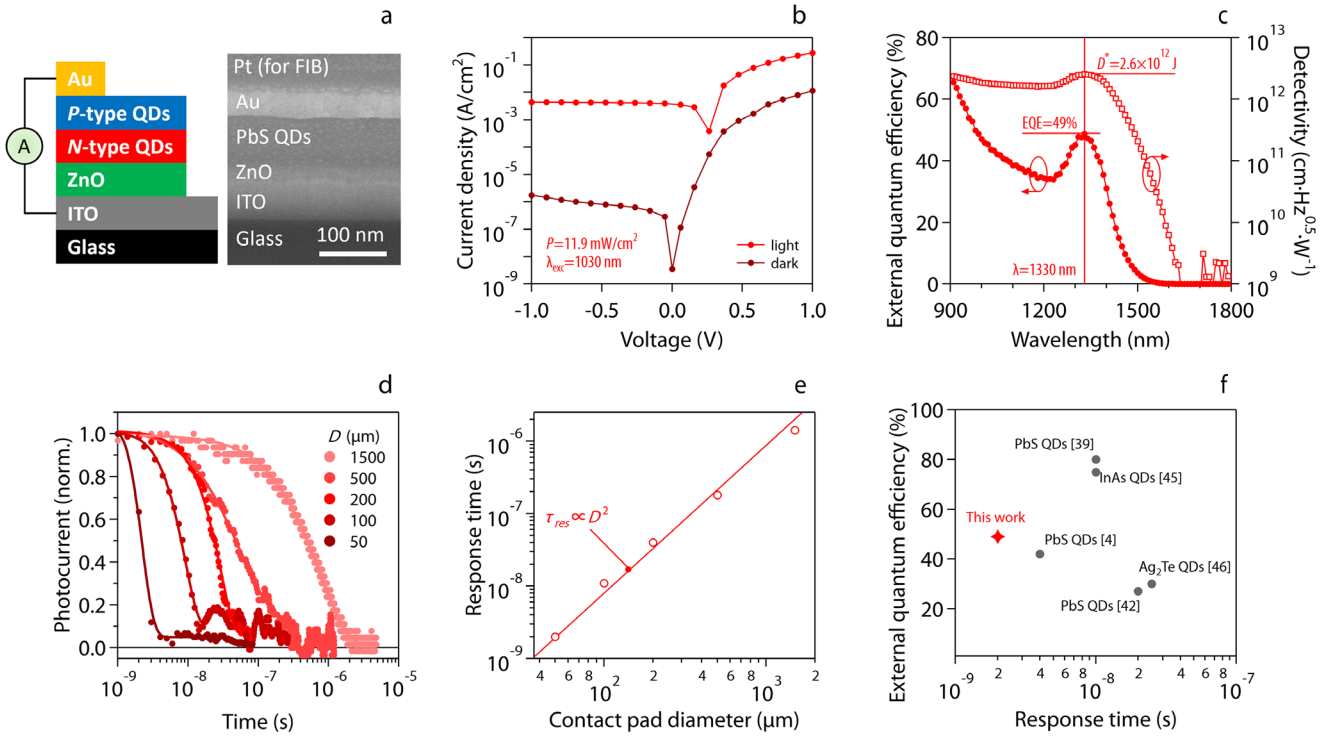

FIGURE 3 | Performance of QDPDs. (a) Diagram and SEM image outlining the cross-section structure of the QDPD stack. (b) *J–V* curve in the dark and under illumination with a 1050 nm LED. (c) Spectrum of the (filled dots) external quantum efficiency and (open squares) the specific detectivity recorded at 0 V bias of the QDPD stack with 1500 μm diameter, highlighting the maximum efficiency and detectivity at 1330 nm. (d) Transient photocurrent after illumination using a 150 fs, 1030 nm laser pulse of QDPDs formed with contact pads of varying diameter as indicated. Full lines are interpolations of the experimental data. (e) Response time as a function of the contact pad diameter. The full line represents a D^2 trendline, in line with the relation expected for τ_{RC}. (f) Diagram comparing the QDPD reported in this work with state-of-the-art devices in terms of EQE and response time. Only photodiodes active within the SWIR and with response times in the range 1–100 ns are included. [Correction added on July 30, 2026, after first online publication: Figure 3 and Figure 4 has been updated.]

barrier that lowers the dark current and suppresses charge-carrier recombination mediated through the gold contact [43]. Details regarding the fabrication process are provided in the Methods section. The scanning electron microscopy (SEM) cross-section of a representative device stack displayed in Figure 3a confirms that this approach yields the intended stack, where the total *n*-PbS/*p*-PbS QD film has a thickness of 100 nm. Additionally, Section S6 provides an optical photograph of a device chip showing gold pads with various diameters defining single devices. Figure 3b displays the current–voltage (*J–V*) characteristics of a representative QDPD with 1500 μm diameter in the dark and illuminated with 1030 nm light at a power density as 14.3 mW/cm^2. Notably, even though the increased internal electric field across the active layer makes trap-assisted tunneling more prominent compared to thicker devices [44], the dark current density remains as low as 2.5×10^{-6} A/cm^2 at − 1 V. Furthermore, the + 1/ − 1 V rectification ratio amounts to 4600, and the photocurrent is nearly voltage independent between 0 and − 1 V reverse bias.

As a rule of thumb, thinner QD layers will absorb less light, thereby reducing the quantum efficiency and detectivity of QDPDs with ultrathin absorber layers. As discussed in Section S7, the QDPDs presented in this study circumvent this issue through the formation of a Fabry–Perot cavity within the QDPD stack. The interference within the layered QDPD stack between incident light and light reflected by the gold surface enhances the optical field in parts of the QDPD stack, mostly notably the *n*-PbS photoactive film, thereby increasing the light absorption by the device. Based on optical simulations, we estimate that the light absorption by a 50 nm QD layer at 1330 nm increases from 16.0% for the film on glass, to 48.4% for the same film within the QDPD, that is, a 3-fold enhancement. Experimentally, we measured a maximal EQE of 49% under 0 V bias at approximately 1330 nm, a wavelength corresponding to the band-gap transition of the n-type PbS QDs, see Figure 3c. In agreement with optical simulations, similar devices with a 30 or 80 nm thick QD films show a lower EQE, while the EQE depends little on the incident, see Section S7. Furthermore, as shown in Section S8, this EQE is power-independent within the range of input powers considered in this study. In combination with the noise current, we calculated a maximum detectivity D^* of 2.6×10^{12} cm · Hz$^{0.5}$ · W^{-1} at 1330 nm for devices with a 1500 μm contact pad (Figure 3c). Notably, scaling the active area down to a 50 μm diameter leaves the EQE unchanged—confirming that the strong built-in field enables rapid vertical charge extraction—while keeping a high D^* of 1.2×10^{12} Jones (Section S9).

Figure 3d displays the transient photocurrent recorded on a series of QDPDs with contact pads of different diameters, held at a bias voltage of 0 V and illumination with a 150 fs pulsed laser at 1030 nm. We used such transients to determine the QDPD response time as the time required for the photocurrent to drop

from 90% to 10% of the initial level. Most interestingly, reducing the contact pad diameter to 50 μm led to response time of just 2 ns, in agreement with the estimates that for such small contact pads, response times of a few ns can be obtained, see Figure 1b. This reduction agrees largely with the expected scaling of τ_{RC} with the contact pad area, see Figure 3e, a regime that is extended to shorter response times in higher mobility films. Figure 3f compiles the performance of SWIR-active QDPDs from literature and the results obtained in this work in terms of EQE and response time [4, 39, 42, 45, 46]. As can be seen, a 2 ns response time is the shortest reported in literature for such QDPDs, and brings QDPDs at the edge of the ns-level response times required for LiDAR applications with submeter spatial resolution and GHz frame rates. Interestingly, to the best of our knowledge, a response time of 2 ns is the shortest ever reported for any colloidal QDPD, regardless of the wavelength range of operation.

1.4 | Nanosecond-Response LEDs Under Electrical-Driven Emission Mode

As illustrated in Figure 1a, carriers are injected under forward bias through the electron (ZnO) and hole (*p*-PbS/Au) contacts into the active layer (*n*-PbS), where they may recombine and thereby emit light. For the given stack, the *p*-PbS film acts as an electron barrier that promotes electroluminescent electron-hole recombination by concentrating electrons in the *n*-PbS layer. Figure 4a shows the injection current density and output power of QDLED device as a function of applied voltage, confirming that an electroluminescent signal appears upon increasing the forward bias. The electroluminescence spectrum is narrow—170 nm full-width-at-half-maximum—and centered around 1442 nm, see Figure 4b. Since this spectrum is similar, albeit somewhat redshifted and broadened, to that of the dispersed QDs used to form the *n*-type layer, see Section S3, we assign the electroluminescence to electron/hole recombination in this layer of the diode stack. As outlined in Section S10, we combined the current density, the output power and the wavelength of the emitted light to determine the EQE of the PbS QDLED as the ratio between the rates of photon emission and carrier injection. According the Figure 4c, the EQE increased with increasing current density—and thus forward bias—and peaked at 8.1% for a current density of 5.7 mA/cm^2. This EQE represents a record value for host-free colloidal PbS QDLEDs in the SWIR region [24, 47]. As shown in Section S10, devices with thicker PbS QD films showed a lower EQE, indicating that for this stack, a 50 nm thick QD film provides an effective balance between detection and emission efficiency. Moreover, area-dependent measurements reveal that while the devices maintain a high peak EQE across different pixel dimensions, the optimal operating point shifts to higher current densities as the area scales down to 50 μm, see Section S10. A radiance of 1.3 W·sr^{-1}·m^{-2} was obtained from the QDLED device at the bias corresponding to the peak EQE, see Figure 4c. Furthermore, the miniaturized 50 μm devices achieve a substantially enhanced maximum radiance of ~70 W·sr^{-1}m^{-2}, possibly related to a better thermal management (Section S11).

We used a custom-built setup to record the transient electroluminescence of the PbS QDLEDs when switching the bias voltage between 0 V and +2 V forward bias, see Section S12 for details. This system has a response time of 9.5 ns, which approaches that of the QDPDs formed using 50 μm contact pads, see Figure 3. As shown in Figure 4d, QDLEDs defined by differently sized contact pads all follow the voltage pulses. However, QDLEDs with smaller contact pads exhibit markedly shorter rise and fall times, see Figure 4e–g. After deconvolution with the instrumental response, see Section S13, we deduced rise and fall times for the 50 μm wide LED of 11.7 and 6.5 ns, respectively. In contrast, the rise and fall time of the 1500 μm wide LED were 150.6 and 52.3 ns. Hence, similar to the QDPD, reducing the capacitance of the device stack results in a faster response that reaches, also in the case of the QDLED, a ns regime. This result is confirmed by a measurement of the 3 dB bandwidth of the QDLEDs of different size, which exceeds 100 MHz for the two smallest devices, see Figure 4h.

When minimizing the capacitive component in the QDLED response by reducing the device size, the 50 μm QDLED exhibits short EL rise and fall times of nanoseconds, see Figure 4g. While lifetime predictions for a QDLED are more complicated than for a QDPD in full depletion under reverse bias, it is interesting to compare such response times with the PL lifetime of the PbS QDs in reference to Equation (2). As shown in Section S14, embedding the PbS QDs within the diode stack reduces the PL lifetime from 0.94 μs to 17 ns. Such a reduction is in good agreement with the maximum 42-fold enhancement expected when the local field increases from 0.07 to 1, and the additional factor of 3 from the dielectric cavity. Alternatively, this more rapid PL transient may reflect competition with non-radiative recombination pathways, for example, related to surface defects induced by the ligand exchange or film formation process. However, the maximum EQE of 8.1%, which was measured without attempts to reduce outcoupling losses, suggests that non-radiative recombination remains limited in the devices presented here, and that the accelerated PL is mostly due to engineering the dielectric environment. Furthermore, in line with Equation (2), the response time of the smallest devices is shorter than the PL lifetime, which suggests that the rapid drift of charge carriers towards the radiative recombination centers further accelerates the switching speed. Note that this point highlights the consistency of the proposed design rules, where short charge-carrier drift times in ultrathin active QD layers can be leveraged for realizing QDPDs and QDLEDs with ns response times.

To the best of our knowledge, the rise and fall times reported in this work are the shortest reported for QDLEDs active at all wavelengths [24, 48–51], see Figure 4i. Achieving such an ns-level performance for the first-time positions QDLEDs at the forefront of nanosecond-scale light sources and Gbs-level communication applications [24, 52, 53]. Furthermore, the reversible switching between QDPD and QDLED operation shown in Section S15 underscores the relevance of such a bifunctional stack for practical applications. For future real-world deployment, thin-film encapsulation serves to maintain long-term device stability. Specifically, atomic layer deposition (ALD) of Al_2O_3 combined with a glass cover can protect the PbS active layer and the top electrode from ambient moisture and oxygen [54]. Finally, the design rules developed here suggest that even faster QDLED operation is achievable when further reducing the active layer thickness, which would, however, come at the expense of detection efficiency in the case of a dual QDPD/QDLED stack.

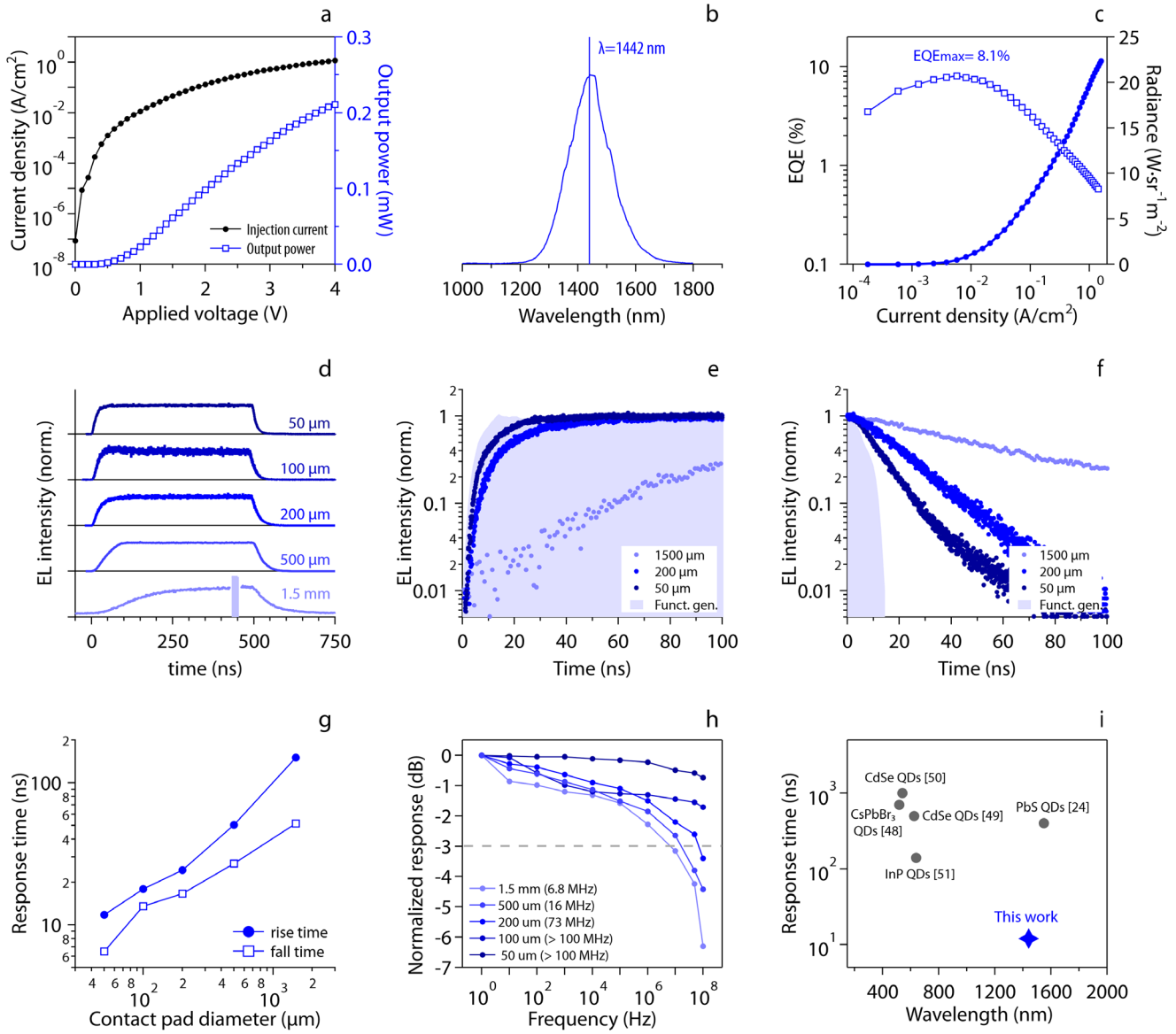

FIGURE 4 | Performance of QDLEDs. (a) The injection current density and output power of QDLED device as a function of applied voltage with 1500 µm diameter pad. (b) Electroluminescence (EL) spectrum of the QDLED with emission peak at 1442 nm, recorded at a bias of 2 V. (c) EQE and radiance of the 1500 µm diameter QDLED device as a function of injection current density. (d) Normalized EL transients recorded on QDLEDs with different contact pad sizes upon pulsing the applied voltage between 0 and + 2 V (forward) bias. (e, f) Zoom on the rising and falling part of the electroluminescence transient for a selection of contact pad diameters. (g) Rise time and fall time of QDLEDs as a function of varying contact pad diameters. (h) Frequency response of the QDLEDs with different device areas. (i) Comparison of the QDLED this work and published data in a wavelength/response time diagram.

2 | Conclusions

In summary, we demonstrate a bifunctional colloidal PbS QD-based diode active at short-wave infrared wavelengths (SWIR) with nanosecond response time. In photodetector mode, the diode a record 2 ns response time, while preserving EQE and detectivity at state-of-the-art levels of 49% and 2.6 × 10^{-12} Jones, respectively. This nanosecond-fast response is brought about by implementation of a QD absorber layer with high electron mobility, an ultrathin structural design, a minimal device capacitance, and an enhancement of the light absorption in the QD film. We argue that similar design principles can shorten the rise and fall time of electroluminescence, and we show that the same stack under forward bias emits SWIR light with an EQE of 8.1% 1.3 W·sr^{-1}·m^{-2} radiance. Furthermore, driving the stack through voltage pulses or an alternating voltage, we demonstrate electroluminescence rise and fall times of 11.7 and 6.5 ns and a 3 dB bandwidth larger 100 MHz for the device with the smallest contact area. These response times in detection and emission mode represent the shortest ever reported among all colloidal QDs. The bifunctional diode stack reported here paves the way to realize simultaneously high spatial imaging resolution, GHz frame-rate, and Gbps optical communication within a monolithic, compact SWIR photonics and bidirectional optical interconnects.

3 | Methods

3.1 | Synthesis of Colloidal QDs

Synthesis of 950 nm PbS QDs. 5.38 g of lead oleate (7.00 mmol, 1.5 equiv.) was dissolved in 25 mL of dry n-octane in a three-neck flask. Simultaneously, 1.70 g (4.67 mmol, 1 equiv.) of N-(3,5-bis(trifluoromethylphenyl))-N'-phenylthiourea was dissolved in 2 mL of diglyme and preheated. Both components were brought to 90 °C under a nitrogen atmosphere before the thiourea solution was rapidly injected into the flask. The mixture was kept at temperature for one minute and then immediately cooled in a water bath.

Synthesis of 1300 nm PbS QDs. 1.54 g of lead oleate (2.00 mmol, 1.33 equiv.) was dissolved in 20 mL n-dodecane and heated to 120°C under nitrogen. In parallel, 0.5828 g of N-(p-(trifluoromethyl)phenyl)-N'-dodecylthiourea (1.5 mmol, 1 equiv.) was mixed with 1 mL of diglyme and preheated. The hot sulfur precursor solution was quickly injected into the lead oleate solution, and the mixture was left to react for 80 s before quenching with a water bath.

In both syntheses, the resulting colloids were purified through at least four cycles of precipitation using acetone and re-dispersion in n-octane. After purification, QDs were filtered through a 0.45 μm membrane and stored in anhydrous n-octane for further use.

3.2 | Device Fabrication

Preparation of zinc oxide nanocrystals (ZnO NCs). ZnO NCs were synthesized using a standard protocol previously reported in the literature [55]. The as-prepared ZnO NCs were dispersed in a 2% (v/v) butylamine solution in chloroform at a concentration of 40 mg/mL. The resulting dispersion was filtered through a 0.45 μm membrane filter and subsequently stored in a refrigerator for future use.

Solution-phase ligand exchange. For the solution-phase ligand exchange process, 345 mg of PbI_2, 110 mg of $PbBr_2$, 18 mg of sodium acetate, and 10 mg of ammonium acetate were dissolved in 7.5 mL of anhydrous N,N-dimethylformamide (DMF) in a 50 mL vial. A diluted solution of oleate-capped PbS quantum dots (OA-PbS) in octane at a concentration of 1.625 mg/mL was then added to the exchange solution. The vial was vigorously shaken for 30 s to promote the transfer of the QDs from the octane to the DMF phase. After phase separation, the octane phase was discarded. To further purify the exchanged QDs, the DMF phase was washed three times with fresh octane. Subsequently, 10 μL of butan-1-amine was added to stabilize the colloidal dispersion. To precipitate the exchanged QDs, 6 mL of toluene (50% v/v) was introduced, followed by centrifugation at 2000 rpm for 2 min. The precipitated QDs were then vacuum-dried for 3 min, a reduced duration likely enabled by more efficient removal of residual organics due to the dual-passivation strategy. Finally, the purified QDs were redispersed in a mixed solvent of 25% DMF and 75% BTA at the desired concentration (50 mg/mL) and was filtered through a 0.45 μm membrane filter for further use.

Diode stack fabrication. Diodes were fabricated on indium tin oxide (ITO) coated glass substrates. The substrates were ultrasonically cleaned sequentially with acetone, ethanol, and deionized water, followed by treatment with O_2 plasma to enhance surface wettability. A ZnO NC solution in chloroform (40 mg mL^{-1}) was spin-coated onto the substrate at 2500 rpm. The QD ink prepared through solution-phase exchange was dynamically spin-coated at 800 rpm for 60 s onto the ZnO layer under a nitrogen atmosphere. The resulting films were then annealed at 80°C for 10 min inside a nitrogen-filled glovebox and subsequently allowed to cool to room temperature prior to proceeding with the next fabrication step. For the second, EDT-exchanged PbS QD layer, colloidal QDs with a concentration of 50 mg/mL were used. The ligand exchange was performed using an ethanedithiol (EDT) solution (0.02 vol% in acetonitrile). Finally, a 100 nm-thick gold (Au) electrode was thermally evaporated onto the PbS QD film.

Solid-state ligand exchange. PbS quantum dots (QDs) were deposited on top of the ZnO layer using a layer-by-layer method. In each cycle, 40 μL of the QD solution was dispensed onto the substrate and spin-coated at 2500 rpm for 30 s. Since oleate-capped QDs are electrically insulating, ligand exchange was performed to replace the long-chain ligands with shorter ones. For the PbS-TBAI layer, a TBAI solution (10 mg mL^{-1} in methanol) was applied for 30 s, followed by spin-coating at 2500 rpm for 10 s. The substrate was then rinsed twice with acetonitrile to remove excess ligands and by-products.

3.3 | Optical and Film Characterizations

The optical absorption measurements under reflection mode were performed with a Perkin-Elmer Lambda 950 UV–Vis-NIR spectrophotometer. The FTIR spectra were measured by a VERTEX 70v vacuum spectrometer (Bruker). Scanning electron microscopy (SEM) images were obtained by a Hitachi S-5200 microscope. The structure and characterization method of FET are shown in Section S5.

3.4 | Device Characterizations

J–V measurements were taken using a sourcemeter (Keithley 2400) under N_2 atmosphere. Wavelength-dependent EQE of QDPD was measured with a quantum efficiency measurement system (Newport Inc.) using a commercial Ge detector as a reference. The noise spectrum was measured by the preamplifier (SR570, SRS) and oscilloscope (DSO8104A Infinium, Agilent). The signal was amplified by 10^8 V/A by a preamplifier and was measured by the oscilloscope under FFT mode. The temporal response of each photodetector was evaluated by measuring the transient photocurrent (TPC) recorded with a 1-GHz oscilloscope (DSO8104A Infinium, Agilent) while a 150-fs pulsed laser (PHAROS, Light Conversion) with a 200-kHz repetition rate illuminated each individual photodetector pixel. All reported TPC experiments were done using a 1030 nm excitation without external bias across the device.

To calculate the EQE of QDLED, the device was placed on top of a calibrated Newport DH-Ge#36319 germanium (Ge)

photodetector, which was connected to a Keithley 2400 for photocurrent measurements. Further experimental details are provided in Section S10. The transient EL was obtained using a home-built setup consisting of a function generator (TGF4162, TTI-aim) shown in Section S12. The transient PL was obtained using a home-built setup consisting of a femtosecond laser. For 3 dB bandwidth measurement, we used a 100 MHz function generator (AFG3102, Tektronix) and connected a detector to read the emission intensity.

Acknowledgements

Z.H., D.V.T., and P.G. acknowledge FWO-Vlaanderen for research funding (FWO projects G0B2921N and G0C5723N). Z.H. acknowledges Ghent University (BOF-GOA24021) for funding. Y.D. acknowledges Ghent University for a postdoctoral research fellowship (BOF23/DOC/027). The work also received funding from the European Research Council (ERC) under the innovation program grant agreement No. 884963 (ERC AdG NARIOS).

Conflicts of Interest

The authors declare no conflicts of interest.

Data Availability Statement

The data that support the findings of this study are available from the corresponding authors upon reasonable request.

References

1. M. P. Hansen and D. S. Malchow, "Overview of SWIR Detectors, Cameras, and Applications," Thermosense XXX 6939 (2008): 69390I https://doi.org/10.1117/12.777776.

2. E. Thimsen, B. Sadtler, and M. Y. Berezin, "Shortwave-Infrared (SWIR) Emitters for Biological Imaging: A Review of Challenges and Opportunities," *Nanophotonics* 6 (2017): 1043–1054, https://doi.org/10.1515/nanoph-2017-0039.

3. O. T. Bruns, T. S. Bischof, D. K. Harris, et al., "Next-Generation in Vivo Optical Imaging With Short-Wave Infrared Quantum Dots," *Nature Biomedical Engineering* 1 (2017): 0056, https://doi.org/10.1038/s41551-017-0056.

4. Y. H. Deng, C. Pang, E. Kheradmand, et al., "Short-Wave Infrared Colloidal QD Photodetector With Nanosecond Response Times Enabled by Ultrathin Absorber Layers," *Advanced Materials* 36 (2024): 2402002, https://doi.org/10.1002/adma.202402002.

5. T. Rauch, M. Böberl, S. F. Tedde, et al., "Near-Infrared Imaging With Quantum-Dot-Sensitized Organic Photodiodes," *Nature Photonics* 3 (2009): 332–336, https://doi.org/10.1038/nphoton.2009.72.

6. Z. Ren, J. Sun, H. Li, et al., "Bilayer PbS Quantum Dots for High-Performance Photodetectors," *Advanced Materials* 29 (2017): 1702055, https://doi.org/10.1002/adma.201702055.

7. X. Tang, M. M. Ackerman, M. Chen, and P. Guyot-Sionnest, "Dual-Band Infrared Imaging Using Stacked Colloidal Quantum Dot Photodiodes," *Nature Photonics* 13 (2019): 277–282, https://doi.org/10.1038/s41566-019-0362-1.

8. D. Shin, F. Xu, D. Venkatraman, et al., "Photon-Efficient Imaging With a Single-Photon Camera," *Nature Communications* 7 (2016): 12046, https://doi.org/10.1038/ncomms12046.

9. J. Yu, J. Zheng, H. Chen, et al., "Near-Infrared Photodetectors Based on $CH_3NH_3PbI_3$ Perovskite Single Crystals for Bioimaging Applications," *Journal of Materials Chemistry C* 10 (2021): 274–280, https://doi.org/10.1039/D1TC04961E.

10. N. Oh, B. H. Kim, S.-Y. Cho, et al., "Double-Heterojunction Nanorod Light-Responsive LEDs for Display Applications," *Science* 355 (2017): 616–619, https://doi.org/10.1126/science.aal2038.

11. C. Bao, Z. Yuan, W. Niu, et al., "A Multifunctional Display Based on Photo-Responsive Perovskite Light-Emitting Diodes," *Nature Electronics* 7 (2024): 375–382, https://doi.org/10.1038/s41928-024-01151-x.

12. Y. Shen, X. Xue, A. H. Jones, et al., "Near 100% External Quantum Efficiency 1550-nm Broad Spectrum Photodetector," *Optics Express* 30 (2022): 3047, https://doi.org/10.1364/OE.447091.

13. B. Depreter, S. Verstuyft, I. Moerman, R. Baets, and P. Van Daele, "presented at Conference Proceedings. Eleventh International Conference on Indium Phosphide and Related Materials (IPRM'99)(Cat. No. 99CH36362)," (1999).

14. S. Park, P. D. Nguyen, Y. Kim, et al., "Metamorphic InGaAs/InAsPSb Quantum Well Light Emitting Diodes for Operation in the Short-Wave Infrared Region," *Advanced Functional Materials* 34 (2024): 2406355, https://doi.org/10.1002/adfm.202406355.

15. M. V. Kovalenko, L. Manna, A. Cabot, et al., "Prospects of Nanoscience With Nanocrystals," *ACS Nano* 9 (2015): 1012–1057, https://doi.org/10.1021/nn506223h.

16. C. R. Kagan, E. Lifshitz, E. H. Sargent, and D. V. Talapin, "Building Devices From Colloidal Quantum Dots," *Science* 353 (2016): aac5523, https://doi.org/10.1126/science.aac5523.

17. I. Moreels, Y. Justo, B. De Geyter, K. Haustraete, J. C. Martins, and Z. Hens, "Size-Tunable, Bright, and Stable PbS Quantum Dots: A Surface Chemistry Study," *ACS Nano* 5 (2011): 2004–2012.

18. J. Leemans, V. Pejović, E. Georgitzikis, et al., "Colloidal III–V Quantum Dot Photodiodes for Short-Wave Infrared Photodetection," *Advanced Science* 9 (2022): 2200844, https://doi.org/10.1002/advs.202200844.

19. Q. Xu, L. Meng, K. Sinha, F. I. Chowdhury, J. Hu, and X. Wang, "Ultrafast Colloidal Quantum Dot Infrared Photodiode," *ACS Photonics* 7 (2020): 1297.

20. R. Sliz, M. Lejay, J. Z. Fan, et al., "Stable Colloidal Quantum Dot Inks Enable Inkjet-Printed High-Sensitivity Infrared Photodetectors," *ACS Nano* 13 (2019): 11988–11995, https://doi.org/10.1021/acsnano.9b06125.

21. E. Bossavit, D. Mastrippolito, C. Gureghian, et al., "Ultrasharp, Cavity Enhanced, Broadly Tunable Infrared Detection Using Colloidal Quantum Dots," *Nano Letters* 25 (2025): 9485–9491.

22. A. Houtepen, E. Sargent, I. Infante, et al., "Colloidal Quantum Dots for Optoelectronics," *Nature Reviews Methods Primers* 5 (2025): 42, https://doi.org/10.1038/s43586-025-00413-y.

23. V. Pejović, E. Georgitzikis, J. Lee, et al., "Infrared Colloidal Quantum Dot Image Sensors," *Ieee Transactions on Electron Devices* 69 (2021): 2840.

24. S. Pradhan, M. Dalmases, N. Taghipour, B. Kundu, and G. Konstantatos, "Colloidal Quantum Dot Light Emitting Diodes at Telecom Wavelength With 18% Quantum Efficiency and Over 1 MHz Bandwidth," *Advanced Science* 9 (2022): 2200637, https://doi.org/10.1002/advs.202200637.

25. G. Whitworth, M. Dalmases, N. Taghipour, and G. Konstantatos, "Solution-Processed PbS Quantum Dot Infrared Laser With Room-Temperature Tunable Emission in the Optical Telecommunications Window," *Nature Photonics* 15 (2021): 738–742, https://doi.org/10.1038/s41566-021-00878-9.

26. Z. Liu, C. Sun, Q. Wang, et al., "Colloidal InSb Quantum Dots Mid-Wave Infrared Photoconductive Detectors via One-Step Strong Acid Surface Treatment Strategy," *Nano Letters* 25 (2025): 13549–13556, https://doi.org/10.1021/acs.nanolett.5c03048.

27. Y. Chen, B. Zeng, M. Lu, et al., "Elemental Nanocrystal Redox Pathway Enables Antimonide Colloidal Quantum Dots," *Journal of the American Chemical Society* 148 (2026): 13216–13225, https://doi.org/10.1021/jacs.5c23366.

28. X. Zhao, L. J. Lim, S. S. Ang, and Z. K. Tan, "Efficient Short-Wave Infrared Light-Emitting Diodes Based on Heavy-Metal-Free Quantum Dots," *Advanced Materials* 34 (2022): 2206409, https://doi.org/10.1002/adma.202206409.

29. E. Georgitzikis, P. E. Malinowski, Y. Li, et al., "Integration of PbS Quantum Dot Photodiodes on Silicon for NIR Imaging," *IEEE Sensors Journal* 20 (2019): 6841–6848, https://doi.org/10.1109/JSEN.2019.2933741.

30. L. Sun, J. J. Choi, D. Stachnik, et al., "Bright Infrared Quantum-Dot Light-Emitting Diodes Through Inter-Dot Spacing Control," *Nature Nanotechnology* 7 (2012): 369–373, https://doi.org/10.1038/nnano.2012.63.

31. X. Gong, Z. Yang, G. Walters, et al., "Highly Efficient Quantum Dot Near-Infrared Light-Emitting Diodes," *Nature Photonics* 10 (2016): 253–257, https://doi.org/10.1038/nphoton.2016.11.

32. S. M. Sze, *Semiconductor Devices: Physics and Technology* (John wiley & sons, 2008).

33. Z. Hens and I. Moreels, "Light Absorption by Colloidal Semiconductor Quantum Dots," *Journal of Materials Chemistry* 22 (2012): 10406, https://doi.org/10.1039/c2jm30760j.

34. I. Moreels, K. Lambert, D. Smeets, et al., "Size-Dependent Optical Properties of Colloidal PbS Quantum Dots," *ACS Nano* 3 (2009): 3023–3030, https://doi.org/10.1021/nn900863a.

35. C. Cheng, J. Li, and X. Cheng, "Photoluminescence Lifetime and Absorption Spectrum of PbS Nanocrystal Quantum Dots," *Journal of Luminescence* 188 (2017): 252–257, https://doi.org/10.1016/j.jlumin.2017.04.037.

36. C. Zhang, D. Han, and X. Zhang, "PbS Colloidal Quantum Dots: Ligand Exchange in Solution," *Coatings* 14 (2024): 761, https://doi.org/10.3390/coatings14060761.

37. O. Voznyy, D. Zhitomirsky, P. Stadler, Z. Ning, S. Hoogland, and E. H. Sargent, "A Charge-Orbital Balance Picture of Doping in Colloidal Quantum Dot Solids," *ACS Nano* 6 (2012): 8448–8455, https://doi.org/10.1021/nn303364d.

38. P. R. Brown, D. Kim, R. R. Lunt, et al., "Energy Level Modification in Lead Sulfide Quantum Dot Thin Films Through Ligand Exchange," *ACS Nano* 8 (2014): 5863–5872, https://doi.org/10.1021/nn500897c.

39. M. Vafaie, J. Z. Fan, A. M. Najarian, et al., "Colloidal Quantum Dot Photodetectors With 10-ns Response Time and 80% Quantum Efficiency at 1,550 nm," *Matter* 4 (2021): 1042–1053.

40. M. P. Hendricks, M. P. Campos, G. T. Cleveland, I. Jen-La Plante, and J. S. Owen, "A Tunable Library of Substituted Thiourea Precursors to Metal Sulfide Nanocrystals," *Science* 348 (2015): 1226–1230, https://doi.org/10.1126/science.aaa2951.

41. M. Biondi, M. J. Choi, O. Ouellette, et al., "A Chemically Orthogonal Hole Transport Layer for Efficient Colloidal Quantum Dot Solar Cells," *Advanced Materials* 32 (2020): 1906199, https://doi.org/10.1002/adma.201906199.

42. Y.-H. Deng, E. Kheradmand, C. Pang, et al., "Super Bending-Stable Flexible Colloidal QD Photodetector With Fast Response and Near-Unity Carrier Extraction Efficiency," *ACS Applied Materials & Interfaces* 17 (2025): 14243.

43. C.-H. M. Chuang, P. R. Brown, V. Bulović, and M. G. Bawendi, "Improved Performance and Stability in Quantum Dot Solar Cells Through Band Alignment Engineering," *Nature Materials* 13 (2014): 796–801, https://doi.org/10.1038/nmat3984.

44. G.-S. Choi, M. J. Lim, I. Sutcu, et al., "Tailoring of Colloidal Quantum Dot Layer Thickness for Highly Efficient Short-Wavelength Infrared Photodiode," *Applied Physics Letters* 124, no. 12 (2024): 121103, https://doi.org/10.1063/5.0188574.

45. P. Xia, S. Wang, Y. Chen, et al., "Improved Facet and Edge Passivation in Near-Infrared III-V Colloidal Quantum Dot Photodetectors," *Advanced Materials* 37 (2025): 2419020, https://doi.org/10.1002/adma.202419020.

46. Y. Wang, H. Wu, C. Rodà, et al., "Shortwave Infrared Light Detection and Ranging Using Silver Telluride Quantum Dots," *Advanced Materials* 37 (2025): 2500977, https://doi.org/10.1002/adma.202500977.

47. S. Pradhan, F. Di Stasio, Y. Bi, et al., "High-Efficiency Colloidal Quantum Dot Infrared Light-Emitting Diodes via Engineering at the Supra-Nanocrystalline Level," *Nature Nanotechnology* 14 (2019): 72–79, https://doi.org/10.1038/s41565-018-0312-y.

48. Q. Zhang, K. Yang, C. Luo, et al., "Nanosecond Response Perovskite Quantum Dot Light-Emitting Diodes With Ultra-High Resolution for Active Display Application," *Light: Science & Applications* 14 (2025): 285, https://doi.org/10.1038/s41377-025-01959-y.

49. T. Zhou, F. Tian, and S. Chen, "Nanosecond-Pulsed Electroluminescence From High Current–Driven Quantum-Dot Light-Emitting Diodes," *Science Advances* 11 (2025): ads1388, https://doi.org/10.1126/sciadv.ads1388.

50. X. Lu, Y. Deng, S. He, et al., "Accelerated Response Speed of Quantum-Dot Light-Emitting Diodes by Hole-Trap-Induced Excitation Memory," *Nature Electronics* 8 (2025): 331–342.

51. Y. Kim, T. Lee, D. Shin, W. K. Bae, and J. Kwak, "Cd-Free Quantum-Dot Light-Emitting Diodes through Nanometer-Thick ZnS/ZnMgO Double-Electron Transport Layers," *ACS Applied Nano Materials* 8 (2024): 307.

52. F. P. García de Arquer, D. V. Talapin, V. I. Klimov, Y. Arakawa, M. Bayer, and E. H. Sargent, "Semiconductor Quantum Dots: Technological Progress and Future Challenges," *Science* 373 (2021): aaz8541.

53. X. Tang, M. M. Ackerman, and P. Guyot-Sionnest, "Acquisition of Hyperspectral Data With Colloidal Quantum Dots," *Laser & Photonics Reviews* 13 (2019): 1900165, https://doi.org/10.1002/lpor.201900165.

54. R. R. Petit, R. Ozdemir, H. Van Avermaet, et al., "Atomic Layer Deposition for Stable InP-Based On-Chip Quantum Dot microLEDs: Hybrid Quantum Dot Pockets," *ACS Applied Materials & Interfaces* 16 (2024): 63989–64001, https://doi.org/10.1021/acsami.4c11391.

55. W. J. Beek, M. M. Wienk, M. Kemerink, X. Yang, and R. A. Janssen, "Hybrid Zinc Oxide Conjugated Polymer Bulk Heterojunction Solar Cells," *Journal of Physical Chemistry B* 109 (2005): 9505–9516, https://doi.org/10.1021/jp050745x.

Supporting Information

Additional supporting information can be found online in the Supporting Information section.

Supporting File: adma74108-sup-0001-SuppMat.docx.